

Test of Lorentz invariance with atmospheric neutrinos

K. Abe,^{1,29} Y. Haga,¹ Y. Hayato,^{1,29} M. Ikeda,¹ K. Iyogi,¹ J. Kameda,^{1,29} Y. Kishimoto,^{1,29} M. Miura,^{1,29} S. Moriyama,^{1,29} M. Nakahata,^{1,29} Y. Nakano,¹ S. Nakayama,^{1,29} H. Sekiya,^{1,29} M. Shiozawa,^{1,29} Y. Suzuki,^{1,29} A. Takeda,^{1,29} H. Tanaka,¹ T. Tomura,^{1,29} K. Ueno,¹ R. A. Wendell,^{1,29} T. Yokozawa,¹ T. Irvine,² T. Kajita,^{2,29} I. Kametani,² K. Kaneyuki,^{2,29,*} K. P. Lee,² T. McLachlan,² Y. Nishimura,² E. Richard,² K. Okumura,^{2,29} L. Labarga,³ P. Fernandez,³ J. Gustafson,⁴ E. Kearns,^{4,29} J. L. Raaf,⁴ J. L. Stone,^{4,29} L. R. Sulak,⁴ S. Berkman,⁵ H. A. Tanaka,⁵ S. Tobayama,⁵ M. Goldhaber,^{6,*} G. Carminati,⁷ W. R. Kropp,⁷ S. Mine,⁷ P. Weatherly,⁷ A. Renshaw,⁷ M. B. Smy,^{7,29} H. W. Sobel,^{7,29} V. Takhistov,⁷ K. S. Ganezer,⁸ B. L. Hartfiel,⁸ J. Hill,⁸ W. E. Keig,⁸ N. Hong,⁹ J. Y. Kim,⁹ I. T. Lim,⁹ T. Akiri,¹⁰ A. Himmel,¹⁰ K. Scholberg,^{10,29} C. W. Walter,^{10,29} T. Wongjirad,¹⁰ T. Ishizuka,¹¹ S. Tasaka,¹² J. S. Jang,¹³ J. G. Learned,¹⁴ S. Matsuno,¹⁴ S. N. Smith,¹⁴ T. Hasegawa,¹⁵ T. Ishida,¹⁵ T. Ishii,¹⁵ T. Kobayashi,¹⁵ T. Nakadaira,¹⁵ K. Nakamura,^{15,29} Y. Oyama,¹⁵ K. Sakashita,¹⁵ T. Sekiguchi,¹⁵ T. Tsukamoto,¹⁵ A. T. Suzuki,¹⁶ Y. Takeuchi,¹⁶ C. Bronner,¹⁷ S. Hirota,¹⁷ K. Huang,¹⁷ K. Ieki,¹⁷ T. Kikawa,¹⁷ A. Minamino,¹⁷ A. Murakami,¹⁷ T. Nakaya,^{17,29} K. Suzuki,¹⁷ S. Takahashi,¹⁷ K. Tateishi,¹⁷ Y. Fukuda,¹⁸ K. Choi,¹⁹ Y. Ito,¹⁹ G. Mitsuka,¹⁹ P. Mijakowski,³⁴ J. Hignight,²⁰ J. Imber,²⁰ C. K. Jung,²⁰ C. Yanagisawa,²⁰ H. Ishino,²¹ A. Kibayashi,²¹ Y. Koshio,²¹ T. Mori,²¹ M. Sakuda,²¹ R. Yamaguchi,²¹ T. Yano,²¹ Y. Kuno,²² R. Tacik,^{23,31} S. B. Kim,²⁴ H. Okazawa,²⁵ Y. Choi,²⁶ K. Nishijima,²⁷ M. Koshihara,²⁸ Y. Suda,²⁸ Y. Totsuka,^{28,*} M. Yokoyama,^{28,29} K. Martens,²⁹ L. L. Marti,²⁹ M. R. Vagins,^{29,7} J. F. Martin,³⁰ P. de Perio,³⁰ A. Konaka,³¹ M. J. Wilking,³¹ S. Chen,³² Y. Zhang,³² K. Connolly,³³ and R. J. Wilkes³³

(Super-Kamiokande Collaboration)

¹Kamioka Observatory, Institute for Cosmic Ray Research, University of Tokyo,
Kamioka, Gifu 506-1205, Japan

²Research Center for Cosmic Neutrinos, Institute for Cosmic Ray Research, University of Tokyo,
Kashiwa, Chiba 277-8582, Japan

³Department of Theoretical Physics, University Autònoma Madrid, 28049 Madrid, Spain

⁴Department of Physics, Boston University, Boston, Massachusetts 02215, USA

⁵Department of Physics and Astronomy, University of British Columbia,
Vancouver, British Columbia V6T1Z4, Canada

⁶Physics Department, Brookhaven National Laboratory, Upton, New York 11973, USA

⁷Department of Physics and Astronomy, University of California,
Irvine, Irvine, California 92697-4575, USA

⁸Department of Physics, California State University, Dominguez Hills, Carson, California 90747, USA

⁹Department of Physics, Chonnam National University, Kwangju 500-757, Korea

¹⁰Department of Physics, Duke University, Durham, North Carolina 27708, USA

¹¹Junior College, Fukuoka Institute of Technology, Fukuoka, Fukuoka 811-0295, Japan

¹²Department of Physics, Gifu University, Gifu, Gifu 501-1193, Japan

¹³GIST College, Gwangju Institute of Science and Technology, Gwangju 500-712, Korea

¹⁴Department of Physics and Astronomy, University of Hawaii, Honolulu, Hawaii 96822, USA

¹⁵High Energy Accelerator Research Organization (KEK), Tsukuba, Ibaraki 305-0801, Japan

¹⁶Department of Physics, Kobe University, Kobe, Hyogo 657-8501, Japan

¹⁷Department of Physics, Kyoto University, Kyoto, Kyoto 606-8502, Japan

¹⁸Department of Physics, Miyagi University of Education, Sendai, Miyagi 980-0845, Japan

¹⁹Solar Terrestrial Environment Laboratory, Nagoya University, Nagoya, Aichi 464-8602, Japan

²⁰Department of Physics and Astronomy, State University of New York at Stony Brook,
New York 11794-3800, USA

²¹Department of Physics, Okayama University, Okayama, Okayama 700-8530, Japan

²²Department of Physics, Osaka University, Toyonaka, Osaka 560-0043, Japan

²³Department of Physics, University of Regina,

3737 Wascana Parkway, Regina, Saskatchewan S4S0A2, Canada

²⁴Department of Physics, Seoul National University, Seoul 151-742, Korea

²⁵Department of Informatics in Social Welfare, Shizuoka University of Welfare,
Yaizu, Shizuoka 425-8611, Japan

²⁶Department of Physics, Sungkyunkwan University, Suwon 440-746, Korea

²⁷Department of Physics, Tokai University, Hiratsuka, Kanagawa 259-1292, Japan

²⁸The University of Tokyo, Bunkyo, Tokyo 113-0033, Japan

²⁹Kavli Institute for the Physics and Mathematics of the Universe (WPI),

Todai Institutes for Advanced Study, University of Tokyo,

Kashiwa, Chiba 277-8582, Japan

³⁰*Department of Physics, University of Toronto,**60 St. George Street, Toronto, Ontario M5S1A7, Canada*³¹*TRIUMF, 4004 Wesbrook Mall, Vancouver, British Columbia V6T2A3, Canada*³²*Department of Engineering Physics, Tsinghua University, Beijing 100084, China*³³*Department of Physics, University of Washington, Seattle, Washington 98195-1560, USA*³⁴*National Centre For Nuclear Research, 00-681 Warsaw, Poland*

(Received 16 October 2014; published 3 March 2015)

A search for neutrino oscillations induced by Lorentz violation has been performed using 4,438 live-days of Super-Kamiokande atmospheric neutrino data. The Lorentz violation is included in addition to standard three-flavor oscillations using the nonperturbative standard model extension (SME), allowing the use of the full range of neutrino path lengths, ranging from 15 to 12,800 km, and energies ranging from 100 MeV to more than 100 TeV in the search. No evidence of Lorentz violation was observed, so limits are set on the renormalizable isotropic SME coefficients in the $e\mu$, $\mu\tau$, and $e\tau$ sectors, improving the existing limits by up to 7 orders of magnitude and setting limits for the first time in the neutrino $\mu\tau$ sector of the SME.

DOI: [10.1103/PhysRevD.91.052003](https://doi.org/10.1103/PhysRevD.91.052003)

PACS numbers: 11.30.Cp, 14.60.Pq

I. INTRODUCTION

Symmetry under Lorentz transformations is a fundamental feature of both the standard model of particle physics and the general theory of relativity, but violations of this symmetry at or below the Planck scale, $m_P \approx 10^{19}$ GeV, have been predicted in a variety of models, including discrete spacetime structure and space-time foam interactions [1,2]. The direct observation of Lorentz violation (LV) would provide access to this Planck-scale physics [3–6]. The standard model extension [4–8] (SME) is an observer-independent effective field theory with all the features of the standard model and general relativity plus all possible LV terms. Lorentz violation can also include violation of charge-parity-time reversal (CPT) symmetry [9,10]. At experimentally accessible energies, these LV signatures are strongly suppressed by a factor of the order of $m_W/m_P \approx 10^{-17}$, the relative magnitudes of the electroweak and Planck scales [11]. Despite this suppression, numerous experimental techniques have been employed to search for LV phenomena [12–14].

Neutrino oscillations, as an interferometric effect, are a sensitive probe of LV with two possible signatures: sidereal variations, which would be evidence of a preferred spatial direction, and spectral anomalies [15–17]. Previous searches within the SME framework have generally focused on sidereal variations, though they sometimes include time-independent components that only modify the spectrum. They have been performed in short-baseline muon (anti)neutrino beams [18–21], the long-baseline NuMI neutrino beam [22,23], the Double-Chooz reactor experiment [24,25], and in atmospheric neutrinos at Ice Cube [26]. These experiments have generally used either

the short-baseline [11] or perturbative [27] approximations of the SME to set limits on LV parameters and report limits for each parameter independently.

The Super-Kamiokande experiment (SK) [28] is a cylindrical, underground, water-Cherenkov detector, with a fiducial mass of 22.5 kton in the inner detector and an active veto outer detector for tagging cosmic ray muons entering the detector. The atmospheric neutrinos are incident from all directions with path lengths and energies spanning 3 and 6 orders of magnitude, respectively. This wide range in L and E makes atmospheric neutrinos a sensitive tool to probe the coefficients which produce spectral anomalies. The SK data cover such a wide range of lengths and energies that the perturbative SME can no longer be used and the exact Hamiltonian must be diagonalized [29]. Since the oscillation of massive neutrinos has been well established in numerous experiments [30–47], the exact Hamiltonian includes three-flavor oscillations and Mikheyev-Smirnov-Wolfenstein (MSW) matter effects [48] in addition to LV. We investigate the real and imaginary parts of the lowest-order effective CPT -even and CPT -odd LV coefficients in the $e\mu$, $\mu\tau$, and $e\tau$ sectors. We are the first neutrino experiment to study isotropic LV in the $\mu\tau$ sector of the SME; all previous experiments sensitive to this sector searched only for sidereal variations.

The neutrino oscillation probability, whether from standard oscillations or Lorentz violation, depends on the initial neutrino flavor, the distance the neutrino travels, L , and the neutrino energy, E . We separate our data into samples correlated with energy and with enhanced ν_μ , ν_e or neutral current (NC) flavor content. The events fully contained (FC) within the inner detector have the lowest energies. Events that start in the inner detector but then exit before depositing all their energy are classified as partially contained (PC) and have generally have higher

*Deceased.

energies. The up-going muon events (UP- μ) that enter the detector having deposited some of their energy in the surrounding rock beforehand are the highest energy sample. This sample only contains up-going events to avoid the overwhelming background of down-going cosmic ray muons. While the energy of the muons cannot be determined event by event, the highest-energy muons will shower inside the detector and can be identified using the method described in [49].

We then further bin the data using observables correlated with L and E . Instead of path length, we bin the data in zenith angle, $\cos \theta_z$, defined as the angle between the event direction and the downward vertical direction. The neutrinos with the shortest path lengths are downward-going ($\cos \theta_z$ near 1) and the neutrinos with the longest path lengths are upward-going ($\cos \theta_z$ near -1). The simulation which predicts the number of neutrino events in each bin includes a distribution of neutrino production heights based on a model of the atmosphere described in more detail in [50]. This range of production heights introduces a smearing of the oscillation probability for a given zenith angle for downward-going and horizontal events but is negligible for upward-going events which cross most of the Earth. For events with one visible Cherenkov ring, we bin in momentum, which is reconstructed using the total amount of light with a 70° cone, and then refined using templates from simulation. For multiring events, partially contained events, and stopping UP- μ events, we bin in visible energy, defined as the energy of an electron that would produce the same total amount of light seen in the detector. The data are divided into a total of 480 bins for each run period, which are then combined across run periods before fitting. The binning is chosen so that enough events are expected in each bin for the fit to be stable. The binning scheme is largely the same as that used for the standard three-flavor oscillation analysis [51], with some upgrades described in [52].

The various data samples and the SK-I through SK-IV data used in this analysis are described in detail in [52], the event generator, Monte Carlo simulation (MC), and reconstruction are described in [50], and recent improvements are described in [53].

II. LORENTZ VIOLATION IN NEUTRINO OSCILLATIONS

In the SME, Lorentz violation is included with neutrino oscillations by adding an LV term, H_{LV} , to the standard neutrino Hamiltonian,

$$H = U M U^\dagger + V_e + H_{LV}, \quad (2.1)$$

where U is the Pontecorvo–Maki–Nakagawa–Sakata mixing (PMNS) matrix [54], M is the neutrino mass matrix,

TABLE I. Lorentz-violating coefficients and their properties. The last row includes all possible combinations of X, Y, Z , and T except TT . d refers to the dimension of the operator. α and β range over the neutrino flavors, e, μ , and τ . The X, Y , and Z indicate coefficients which introduce effects in a particular direction in a Lorentz-violating preferred reference frame. The T and TT terms are not associated with any direction and thus introduce isotropic distortions in the oscillation pattern.

Coefficient	Unit	d	CPT	Oscillation effect
Isotropic				
$a_{\alpha\beta}^T$	GeV	3	Odd	$\propto L$
$c_{\alpha\beta}^{TT}$...	4	Even	$\propto LE$
Directional				
$a_{\alpha\beta}^X, a_{\alpha\beta}^Y, a_{\alpha\beta}^Z$	GeV	3	Odd	Sidereal variation
$c_{\alpha\beta}^{XX}, c_{\alpha\beta}^{YZ}, \dots$...	4	Even	Sidereal variation

$$M = \frac{1}{2E} \begin{pmatrix} 0 & 0 & 0 \\ 0 & \Delta m_{21}^2 & 0 \\ 0 & 0 & \Delta m_{31}^2 \end{pmatrix}, \quad (2.2)$$

and V_e is the electron potential which introduces matter effects [48],

$$V_e = \pm \sqrt{2} G_F \begin{pmatrix} N_e & 0 & 0 \\ 0 & 0 & 0 \\ 0 & 0 & 0 \end{pmatrix}, \quad (2.3)$$

where G_F is the Fermi constant and N_e is the average electron density along the neutrino's path, calculated using the four-layer Primary Reference Earth Model (PREM) of the density profile of the Earth [55].

The Lorentz-violating Hamiltonian, H_{LV} , has many possible terms with complex coefficients summarized in Table I, broadly categorized as isotropic or directional. While in principle atmospheric neutrinos are sensitive to the sidereal variations induced by the directional terms [26], in this analysis we focus only on the isotropic terms which introduce spectral variations which oscillate depending on L and LE (as opposed to the L/E dependence of standard oscillations [56]). The diagonal elements of H_{LV} have also been neglected since they cannot be observed in oscillations, giving

$$H_{LV} = \begin{pmatrix} 0 & a_{e\mu}^T & a_{e\tau}^T \\ (a_{e\mu}^T)^* & 0 & a_{\mu\tau}^T \\ (a_{e\tau}^T)^* & (a_{\mu\tau}^T)^* & 0 \end{pmatrix} - \frac{4E}{3} \begin{pmatrix} 0 & c_{e\mu}^{TT} & c_{e\tau}^{TT} \\ (c_{e\mu}^{TT})^* & 0 & c_{\mu\tau}^{TT} \\ (c_{e\tau}^{TT})^* & (c_{\mu\tau}^{TT})^* & 0 \end{pmatrix} \quad (2.4)$$

for neutrinos. For antineutrinos, the a^T parameters go to $-(a^T)^*$ and the c^{TT} parameters go to $(c^{TT})^*$, which is equivalent to $\text{Re}(a^T) \rightarrow -\text{Re}(a^T)$ and $\text{Im}(c^{TT}) \rightarrow -\text{Im}(c^{TT})$.

A common approach in neutrino oscillation experiments is to treat H_{LV} as a small perturbation δh on the standard model Hamiltonian [27] and calculate the lowest order nonzero variations in the oscillation probability (first order when standard oscillations are present, second order when they are not, such as at short baselines). The sensitivity of Super-K to this model was evaluated [29]. However, for this approach to be valid the perturbation must be small, defined as $|\delta h| \ll 1/L$. If we take the condition as $|\delta h| < 10\% \times (1/L)$, then more than 30% of the events in SK fail this perturbative condition for $a^T = 5 \times 10^{-24}$ GeV, resulting in unphysical oscillation probabilities greater than one and less than zero. Since the events failing the condition belong to the samples most sensitive to Lorentz-violation effects, this model was deemed inappropriate for the Super-K atmospheric neutrino analysis. Instead, we use an exact diagonalization of H which produces bounded oscillation probabilities in Super-K samples for all values of the Lorentz-violating coefficients, shown in detail in Appendix A. The accuracy of this calculation was ensured by confirming that the oscillation probabilities from the full diagonalization matched the standard three-flavor oscillation calculation used in SK (based on [57]) and the perturbative calculations for parameter values that were valid in the perturbative scheme.

Figure 1 shows examples of the ν_μ survival probability vs energy and path length for the a^T and c^{TT} parameters in the $\mu\tau$ sector. Standard oscillations appear as lines of constant L/E , which have slope one on these log-log plots. The $a_{\mu\tau}^T$ and $a_{e\mu}^T$ coefficients create oscillation patterns in ν_μ disappearance that depend only on length. These oscillations will appear as horizontal lines, which can be seen in Fig. 1(b) at high energies where there are no L/E oscillations. The distance (or equivalently $\cos\theta_z$) at which the LV oscillation begin is set by the value of a^T . The $c_{\mu\tau}^{TT}$ and $c_{e\mu}^{TT}$ coefficients introduce LE oscillations which will appear as lines with slope minus one, which can be seen at high energies in Fig. 1(c). The value of c^{TT} controls the energy the new oscillations begin at.

The samples most sensitive to the high-energy $\mu\tau$ signatures are the UP- μ samples. Figure 2 shows the zenith-angle distributions of the three UP- μ data samples, as ratios relative to standard oscillations, compared with the MC predictions corresponding $a_{\mu\tau}^T = 10^{-22}$ GeV and $c_{\mu\tau}^{TT} = 7.5 \times 10^{-23}$ (the same as the examples in Fig. 1). The length-only oscillations from $a_{\mu\tau}^T$ appear as large, zenith-dependent oscillations in the nonshowering and showering UP- μ samples since $\cos\theta_z$ is monotonically (though not linearly) related to distance. The fast oscillations at high energy from $c_{\mu\tau}^{TT}$ create significant extra ν_μ

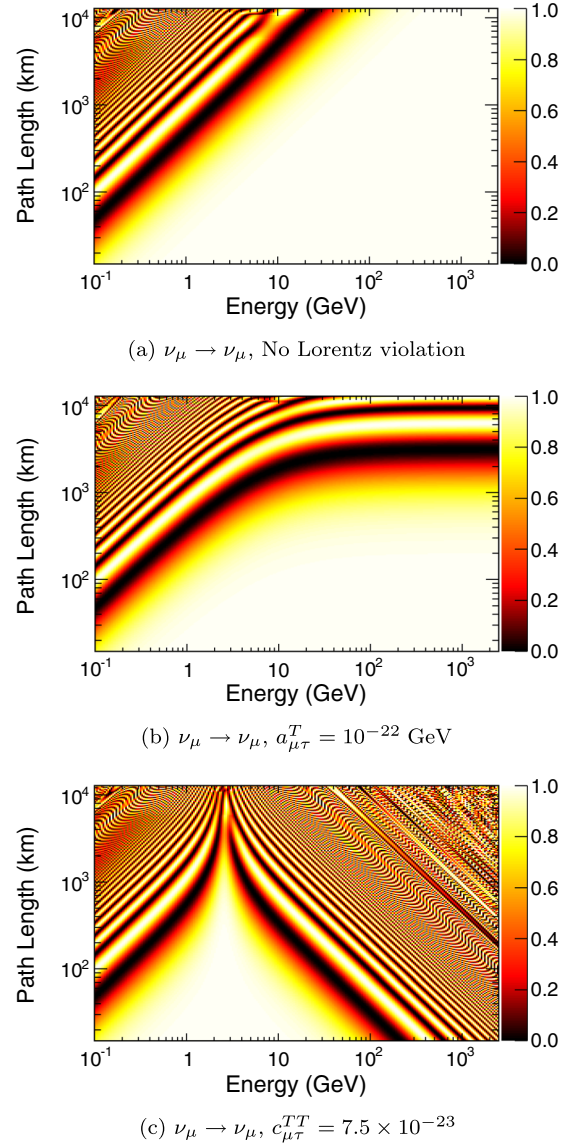


FIG. 1 (color online). The $\nu_\mu \rightarrow \nu_\mu$ oscillation probabilities, plotted in path length vs neutrino energy. (a) Standard oscillations appear as lines of constant L/E which have slope 1 on this log-log scale. Standard three-flavor oscillations are concentrated in the upper-left portion in all three oscillograms, corresponding to low energy and long distance. (b) The $a_{\mu\tau}^T$ coefficient introduces oscillations proportional to L , which appear as horizontal lines (constant L) at high energies. (c) The $c_{\mu\tau}^{TT}$ coefficient introduces LE oscillations which appear as lines with slope minus one. Oscillograms for all sectors, as well as the $\mu \rightarrow e$ probabilities are shown in Appendix B.

disappearance at all $\cos\theta_z$'s in the same through-going samples.

Plots of the ν_μ survival probabilities and the $\nu_\mu \rightarrow \nu_e$ oscillation probabilities for all the a^T and c^{TT} parameters can be seen in Appendix B and the zenith distributions of all the samples compared with the data can be seen in

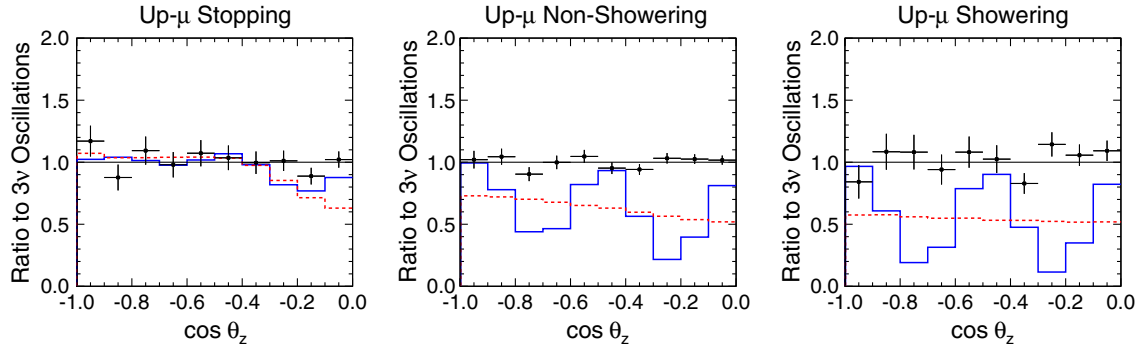


FIG. 2 (color online). Ratios of the summed SK-I through SK-IV $\cos \theta_z$ distributions relative to standard three-flavor oscillations for the UP- μ subsamples, which are the most sensitive to the effects of LV. The stopping subsample (left) contains neutrinos with energies peaking around 10 GeV, the nonshowering subsample (center) peaks around 100 GeV, and the showering subsample (right) peaks around 1 TeV. The black points represent the data with statistical errors. The lines correspond to the MC prediction including Lorentz-violating effects, with $a_{\mu\tau}^T = 10^{-22}$ GeV in solid blue and $c_{\mu\tau}^{TT} = 7.5 \times 10^{-23}$ in dashed red.

Appendix C. Both $a_{e\mu}^T$ and $c_{e\mu}^{TT}$ behave much like their $\mu\tau$ counterpart in the highest energy samples, but also introduce some smaller but significant changes in the lower energy e -like and μ -like samples that would allow the effects of the two sectors to be distinguished from one another. The $a_{e\tau}^T$ and $c_{e\tau}^{TT}$ terms, on the other hand, behave quite differently from the other sectors: they reduce or eliminate L/E oscillations that should otherwise occur at medium and higher energies. So, instead of extra ν_μ disappearance there is less. They also enhance the ν_e appearance signal at lower energies. Oscillograms are only shown for nonzero real parts of the parameters, but the real and imaginary parts produce similar oscillation effects in the high-energy regions where LV-induced oscillations are dominant. The influence of the imaginary parts is only in this high-energy region while the real parts also introduce small modifications in the low-energy oscillation probability.

III. LORENTZ-VIOLATING OSCILLATION ANALYSIS

The three-flavor plus SME oscillation model described in Sec. II is fit to the data samples described above using the techniques from [52]. The fitter minimizes a “pulled” χ^2 [58] assuming Poisson statistics between the MC expectation, calculated for a particular value of the complex coefficient, and the data:

$$\chi^2 = 2 \sum_i \left(\sum_n \tilde{E}_i^{\text{SK}n}(\vec{\theta}, \vec{\epsilon}) - \sum_n \mathcal{O}_i^{\text{SK}n} + \sum_n \mathcal{O}_i^{\text{SK}n} \ln \frac{\sum_n \mathcal{O}_i^{\text{SK}n}}{\sum_n \tilde{E}_i^{\text{SK}n}(\vec{\theta}, \vec{\epsilon})} \right) + \chi_{\text{penalty}}^2(\vec{\epsilon}), \quad (3.1)$$

where n indexes the four SK run periods, i indexes the analysis bins, $\mathcal{O}_i^{\text{SK}n}$ is the number of observed events in bin i during SK n , and $\tilde{E}_i^{\text{SK}n}(\vec{\theta}, \vec{\epsilon})$ is the MC expectation in bin i in SK n with the coefficients being tested, $\vec{\theta}$, and systematic parameters, $\vec{\epsilon}$. The expectation in each bin is calculated separately for each run period and then the run periods are summed for the comparison between data and MC.

The systematic uncertainties are approximated as linear effects on the analysis bins,

$$\tilde{E}_i^{\text{SK}n}(\vec{\theta}, \vec{\epsilon}) = E_i^{\text{SK}n}(\vec{\theta}) \left(1 + \sum_j f_{i,j}^{\text{SK}n} \frac{\epsilon_j}{\sigma_j} \right), \quad (3.2)$$

where j indexes the systematic errors, $E_i^{\text{SK}n}(\vec{\theta})$ is the MC expectation in bin i in SK n without systematic shifts, and $f_{i,j}^{\text{SK}n}$ is the fractional change in bin i in SK n due to σ_j , the 1-sigma change in systematic j . The constraints on these parameters are included as a penalty term in Eq. (3.1):

$$\chi_{\text{penalty}}^2(\vec{\epsilon}) = \sum_j \left(\frac{\epsilon_j}{\sigma_j} \right)^2. \quad (3.3)$$

The analysis includes 155 systematic error parameters. The uncertainties in the atmospheric neutrino flux, neutrino interaction cross sections, particle production within nuclei, and the standard PMNS oscillation parameters are shared across all run periods so $f_{i,j}^{\text{SK}n}$ is the same in SK-I through SK-IV. The uncertainties related to detector performance—reconstruction, particle identification, energy scale, and fiducial volume uncertainties—differ between run periods since they depend on the specific detector geometry and

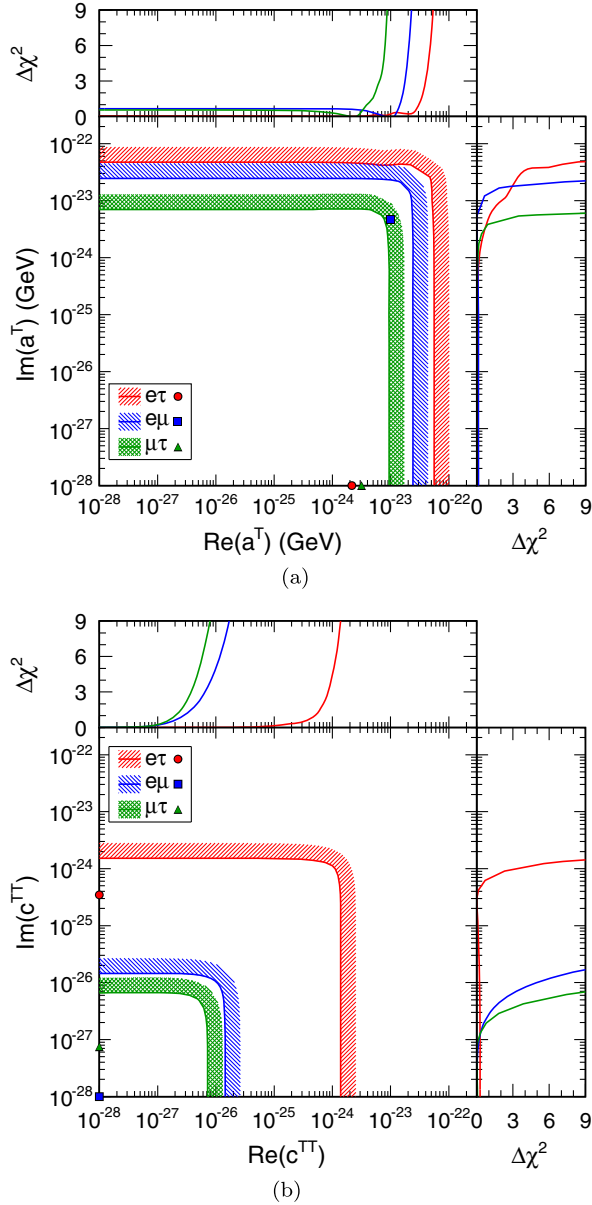


FIG. 3 (color online). Two-dimensional contours at the 95% confidence level for the real and imaginary parts of $a_{e\tau}^T$, $a_{e\mu}^T$, and $a_{\mu\tau}^T$ in (a) and $c_{e\tau}^{TT}$, $c_{e\mu}^{TT}$, and $c_{\mu\tau}^{TT}$ in (b). The hashed areas indicate the side of the contour that is excluded. The best-fit points from the three fits are also shown as markers. The one-dimensional $\Delta\chi^2$ curves are shown in the top and right side plots with the alternate variable profiled out.

hardware. For these uncertainties, $f_{i,j}^{\text{SK}n}$ will be nonzero in only one run period. A table of all systematic uncertainties included in the analysis can be found in the appendix to [52].

In order to focus the analysis on the LV coefficients, the standard oscillation parameters are constrained to external measurements and their uncertainties are taken as

systematic errors. The T2K measurement of ν_μ disappearance, $|\Delta m_{32}^2| = (2.51 \pm 0.10) \times 10^{-3} \text{ eV}^2$ and $\sin^2(\theta_{23}) = 0.514 \pm 0.055$ [59], is used because its narrow-band beam and shorter fixed baseline make it less sensitive to the Lorentz-violating spectral distortions considered in this analysis. The mixing angle $\sin^2(2\theta_{13}) = 0.095 \pm 0.01$ is taken from the 2013 PDG world average [60], the solar terms are taken from the global fit performed by the SK solar +KamLAND analysis, $\Delta m_{21}^2 = (7.46 \pm 0.19) \times 10^{-5} \text{ eV}^2$, $\sin^2(\theta_{12}) = 0.305 \pm 0.021$ [32]. The CP -violating phase δ and the mass hierarchy (the sign of Δm^2) are not yet known and so are allowed to float unconstrained.

Equation (3.1) is minimized with respect to the $\vec{\epsilon}$ for each choice of $\vec{\theta}$ in a fit's parameter space. A set of linear equations in ϵ_j 's is derived from Eq. (3.1) using the fact that the derivative $\partial\chi^2/\partial\epsilon_j$ is zero at the minimum [58]. These equations can then be solved iteratively to find the minimum profile likelihood for that set of oscillation parameters, building up a map of χ^2 vs $\vec{\theta}$. The best fit point is defined as the global minimum of this map.

Six fits are performed for the real and imaginary parts of a^T and c^{TT} in the three sectors, $e\mu$, $e\tau$, and $\mu\tau$. The real and imaginary parts of each coefficient are fit simultaneously, but otherwise the coefficients are fit independently following the procedure typical for SME analyses [12]. Tests with fits to high-statistics fake data sets reliably find no LV when none is present and correctly extract the best fit point if a fake data set with an LV signal is used. However, there is generally some ambiguity between the real and imaginary parts since they produce similar oscillation effects at the energies where LV-oscillations dominate. The low-energy differences allow the correct parameter to be chosen in fits to simulated data with high statistics, but small fluctuations can easily move the best fit point to just the real part, just the imaginary part, or a combination of the two.

No significant evidence of Lorentz violation is seen in any of the fits. The most significant exclusion of no LV is for $a_{e\mu}^T$, and it has a $\Delta\chi^2 = 1.4$, less than 1σ with 2 degrees of freedom. The absolute χ^2 for the fits ranges from 538.6 to 540.0 with 480 bins (477 degrees of freedom), corresponding to goodness-of-fit p -values around 2.5%. The best-fit momentum and zenith distributions for the a^T and c^{TT} fits are shown, compared with the data, in Appendix C. A summary of the fit results, including upper limits at the 95% confidence level, best-fit values, and levels of agreement with no Lorentz violation can be seen in Table II. The two-dimensional contours at the 95% confidence level on a^T and c^{TT} are shown in Figs. 3(a) and 3(b) respectively. The limits on the real and imaginary parts of the parameter are slightly different in the $e\tau$ and $\mu\tau$ sectors because these fits found best fit points with different values for the real and imaginary components.

TABLE II. Summary of the results of the six fits for Lorentz-violating parameters (the real and imaginary parts of each parameter are fit simultaneously). The upper limits at the 95% confidence level (C.L.) and best fits are shown, as well as the $\Delta\chi^2$ between the best fit and the hypothesis of no Lorentz violation. The most significant exclusion of Lorentz invariance is in the $a_{e\mu}^T$ fit, which is still consistent with no LV at the 68% confidence level. Since the parameters are scanned on a logarithmic scale and only positive parameter values are used, 10^{-28} is the minimum value considered and is equivalent to no LV.

LV parameter		Limit at 95% C.L.	Best fit	No LV $\Delta\chi^2$	Previous limit
$e\mu$	$\text{Re}(a^T)$	1.8×10^{-23} GeV	1.0×10^{-23} GeV	1.4	4.2×10^{-20} GeV [61]
	$\text{Im}(a^T)$	1.8×10^{-23} GeV	4.6×10^{-24} GeV		
	$\text{Re}(c^{TT})$	8.0×10^{-27}	1.0×10^{-28}	0.0	9.6×10^{-20} [61]
	$\text{Im}(c^{TT})$	8.0×10^{-27}	1.0×10^{-28}		
$e\tau$	$\text{Re}(a^T)$	4.1×10^{-23} GeV	2.2×10^{-24} GeV	0.0	7.8×10^{-20} GeV [62]
	$\text{Im}(a^T)$	2.8×10^{-23} GeV	1.0×10^{-28} GeV		
	$\text{Re}(c^{TT})$	9.3×10^{-25}	1.0×10^{-28}	0.3	1.3×10^{-17} [62]
	$\text{Im}(c^{TT})$	1.0×10^{-24}	3.5×10^{-25}		
$\mu\tau$	$\text{Re}(a^T)$	6.5×10^{-24} GeV	3.2×10^{-24} GeV	0.9	...
	$\text{Im}(a^T)$	5.1×10^{-24} GeV	1.0×10^{-28} GeV		
	$\text{Re}(c^{TT})$	4.4×10^{-27}	1.0×10^{-28}	0.1	...
	$\text{Im}(c^{TT})$	4.2×10^{-27}	7.5×10^{-28}		

IV. CONCLUSIONS

The large range of energies and path lengths in the atmospheric neutrino sample make it sensitive to a variety of spectral distortions introduced by violations of Lorentz invariance as parametrized by the standard model extension. However, the long distances and high energies make the perturbative approach used in other experiments inappropriate, so we present the first analysis of Lorentz violation in neutrino oscillations where the full, nonperturbative Hamiltonian is used, combined with three-flavor neutrino oscillations. No evidence of LV is seen, so we set limits on the isotropic parameters a^T and c^{TT} in the $e\mu$, $\mu\tau$, and $e\tau$ sectors. These are the first limits on the isotropic parameters in the $\mu\tau$ sector, and we improve the existing limits [12] on a^T by 3 orders of magnitude and on c^{TT} by 7 orders of magnitude thanks to the wide range of energies and path lengths of the neutrinos in the atmospheric neutrino samples. Future studies of SK atmospheric neutrino data could also set limits on the directional parameters by searching for sidereal variations in the atmospheric neutrino data.

ACKNOWLEDGMENTS

We would like to thank A. Kosteletzky for his advice and support and we are grateful to J. S. Diaz for working closely with us to calculate and implement the Lorentz-violating oscillation probabilities. The authors gratefully acknowledge the cooperation of the Kamioka Mining and Smelting Company. Super-K has been built and operated from funds provided by the Japanese Ministry of Education, Culture, Sports, Science and Technology, the U.S. Department of Energy, and the U.S. National Science Foundation. This work was partially supported by the Research Foundation of Korea (BK21 and KNRC), the Korean Ministry of

Science and Technology, the National Science Foundation of China, the European Union FP7 (DS laguna-lbno PN-284518 and ITN invisibles GA-2011-289442), the National Science and Engineering Research Council (NSERC) of Canada, and the Scinet and Westgrid consortia of Compute Canada.

APPENDIX A: NEUTRINO OSCILLATIONS WITH LORENTZ VIOLATION

This Appendix shows the full calculation of the neutrino oscillation probabilities with both three-neutrino mixing and Lorentz Violation, without assuming that the baseline is short or that the LV Hamiltonian is small. Neither of these approximations is valid for SK because of its wide range of path lengths and energies.

The oscillation probabilities for Lorentz violation plus three-flavor oscillations including matter effects are calculated by diagonalizing the Hamiltonian which includes all these pieces, following the method from [63]. Combining the parts described individually in Sec. II,

$$\begin{aligned}
 H = & U \begin{pmatrix} 0 & 0 & 0 \\ 0 & \frac{\Delta m_{21}^2}{2E} & 0 \\ 0 & 0 & \frac{\Delta m_{31}^2}{2E} \end{pmatrix} U^\dagger \pm \sqrt{2} G_F \begin{pmatrix} N_e & 0 & 0 \\ 0 & 0 & 0 \\ 0 & 0 & 0 \end{pmatrix} \\
 & \pm \begin{pmatrix} 0 & a_{e\mu}^T & a_{e\tau}^T \\ (a_{e\mu}^T)^* & 0 & a_{\mu\tau}^T \\ (a_{e\tau}^T)^* & (a_{\mu\tau}^T)^* & 0 \end{pmatrix} - \frac{4E}{3} \begin{pmatrix} 0 & c_{e\mu}^{TT} & c_{e\tau}^{TT} \\ (c_{e\mu}^{TT})^* & 0 & c_{\mu\tau}^{TT} \\ (c_{e\tau}^{TT})^* & (c_{\mu\tau}^{TT})^* & 0 \end{pmatrix}, \quad (A1)
 \end{aligned}$$

where U is the PMNS mixing matrix, E is the neutrino energy, G_F is Fermi's constant, and N_e is the average

electron density along the neutrino's path. For antineutrinos, the complex conjugates of all terms are taken (though in practice this only affects δ_{cp} in U and the a and c parameters) and the signs of the ν_e matter effect and a matrices are negative.

The next step is to diagonalize this 3×3 matrix to calculate the new eigenvalues and mixing matrix. Since the Hamiltonian is Hermitian the eigenvalues are guaranteed to be real. They can be calculated below as the roots of a cubic equation,

$$E_i = -2\sqrt{Q} \cos\left(\frac{\theta_i}{3}\right) - \frac{a}{3}, \quad (\text{A2})$$

with $i = 0, 1, 2$ and where the components Q and θ_i ,

$$Q = \frac{a^2 - 3b}{9}, \quad (\text{A3})$$

$$\theta_0 = \cos^{-1}(RQ^{-\frac{3}{2}}), \quad (\text{A4})$$

$$\theta_1 = \theta_0 + 2\pi, \quad (\text{A5})$$

$$\theta_2 = \theta_0 - 2\pi, \quad (\text{A6})$$

can be calculated from the trace and determinant of H :

$$a = -\text{Tr}(H), \quad (\text{A7})$$

$$b = \frac{\text{Tr}(H)^2 - \text{Tr}(H^2)}{2}, \quad (\text{A8})$$

$$c = -\det(H), \quad (\text{A9})$$

$$R = \frac{2a^3 - 9ab + 27c}{54}. \quad (\text{A10})$$

The diagonalization also produces a mixing matrix U ,

$$U_{ei} = \frac{B_i^* C_i}{N_i}, \quad U_{\mu i} = \frac{A_i C_i}{N_i}, \quad U_{\tau i} = \frac{A_i B_i}{N_i}, \quad (\text{A11})$$

where

$$A_i = H_{\mu\tau}(H_{ee} - E_i) - H_{\mu e}H_{e\tau}, \quad (\text{A12})$$

$$B_i = H_{\tau e}(H_{\mu\mu} - E_i) - H_{\tau\mu}H_{\mu e}, \quad (\text{A13})$$

$$C_i = H_{\mu e}(H_{\tau\tau} - E_i) - H_{\mu\tau}H_{\tau e}, \quad (\text{A14})$$

$$N_i^2 = |A_i B_i|^2 + |A_i C_i|^2 + |B_i C_i|^2. \quad (\text{A15})$$

The oscillation probabilities can then be calculated from

$$P_{\alpha\beta} = |\langle \nu_\beta | e^{-iHL} | \nu_\alpha \rangle|^2 \quad (\text{A16})$$

which expands to

$$P_{\alpha\beta} = \delta_{\alpha\beta} - 4 \sum_{j>i} \text{Re}(U_{\beta j} U_{\beta i}^* U_{\alpha j}^* U_{\alpha i}) \sin^2(L\Delta E_{ji}/2) + 2 \sum_{j>i} \text{Im}(U_{\beta j} U_{\beta i}^* U_{\alpha j}^* U_{\alpha i}) \sin^2(L\Delta E_{ji}), \quad (\text{A17})$$

where $\Delta E_{ji} = E_j - E_i$ are the differences between the eigenvalues.

We can expand further, taking two examples particularly relevant for atmospheric neutrinos. The ν_μ survival probability,

$$P_{\mu\mu} = 1 - \sum_{j>i} \frac{|A_j A_i C_j C_i|^2}{N_j^2 N_i^2} \sin^2(L\Delta E_{ji}/2), \quad (\text{A18})$$

and the ν_e appearance probability,

$$P_{\mu e} = -4 \sum_{j>i} \frac{\text{Re}(A_j^* A_i B_j^* B_i) |C_j C_i|^2}{N_j^2 N_i^2} \sin^2(L\Delta E_{ji}/2) + 2 \sum_{j>i} \frac{\text{Im}(A_j^* A_i B_j^* B_i) |C_j C_i|^2}{N_j^2 N_i^2} \sin(L\Delta E_{ji}). \quad (\text{A19})$$

APPENDIX B: OSCILLOGRAMS

This Appendix includes plots of the $\nu_\mu \rightarrow \nu_\mu$ and $\nu_\mu \rightarrow \nu_e$ oscillation probabilities vs neutrino path length and neutrino energy for standard three-flavor oscillations (Fig. 4) and for large (10^{-22} GeV and 7.5×10^{-23}) values of the LV parameters (Figs. 5-6) to show the effects of the six different coefficients. Oscillograms for standard three-flavor oscillations are included for comparison at the end. For both a^T and c^{TT} , the $e\mu$ and $\mu\tau$ sectors have similar $\nu_\mu \rightarrow \nu_\mu$ probabilities but different $\nu_\mu \rightarrow \nu_e$ probabilities. For both parameters the $e\tau$ sector has the opposite effect of the other sectors: eliminating standard oscillations instead of introducing nonstandard oscillations.

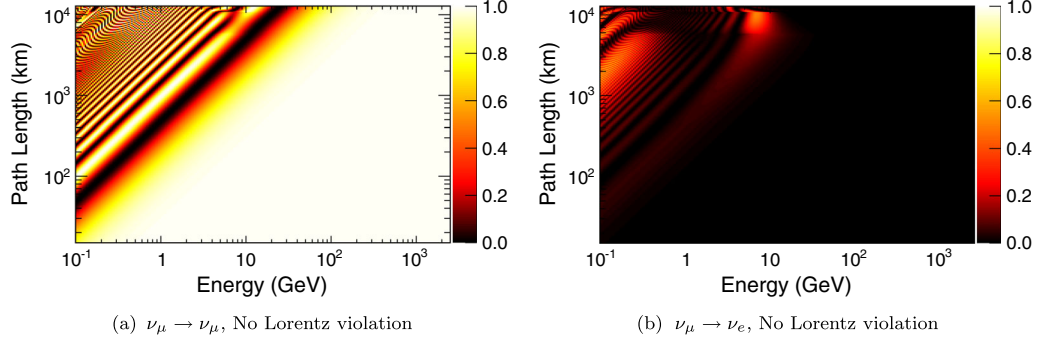


FIG. 4 (color online). For comparison, the $\nu_\mu \rightarrow \nu_\mu$ (left) and $\nu_\mu \rightarrow \nu_e$ (right) oscillation probabilities, plotted in path length vs neutrino energy for standard three-flavor oscillations.

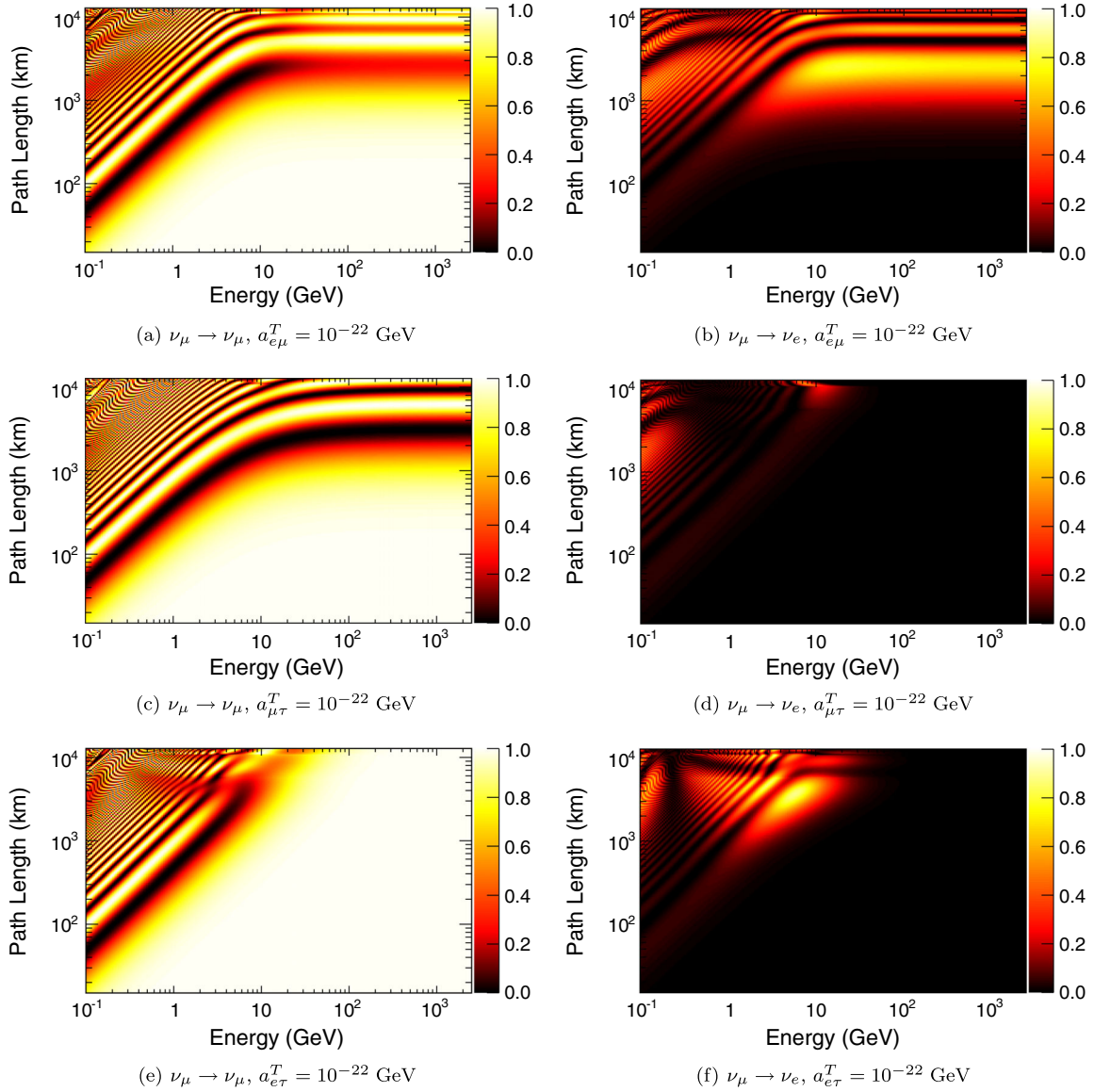


FIG. 5 (color online). The $\nu_\mu \rightarrow \nu_\mu$ (left) and $\nu_\mu \rightarrow \nu_e$ (right) oscillation probabilities, plotted in path length vs neutrino energy for the a^T parameter in the (top to bottom) $e\mu$, $\mu\tau$, and $e\tau$ sectors. The a^T coefficients scale terms proportional to L , so the distortions get stronger as $\cos\theta_z$ approaches -1 .

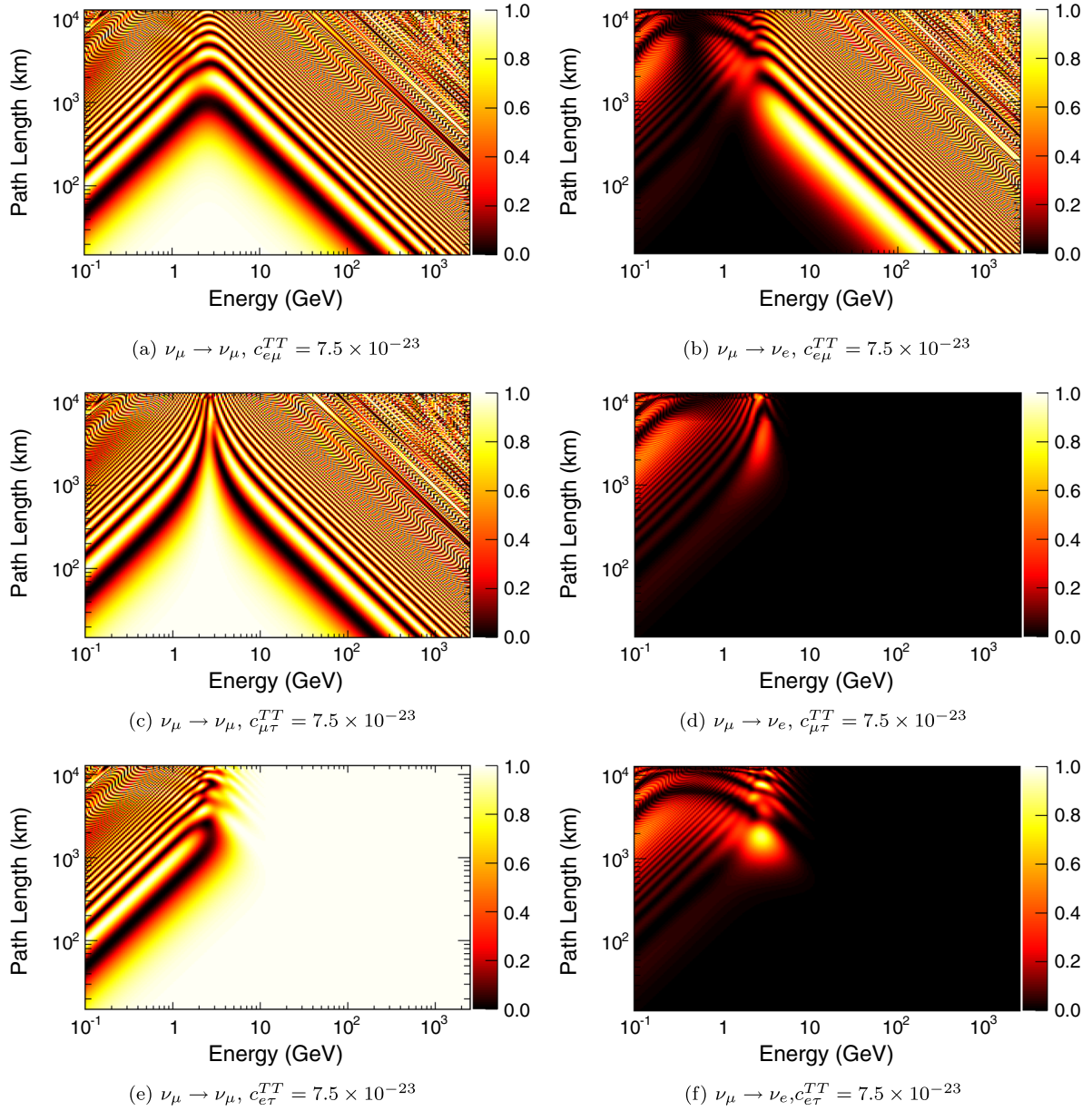


FIG. 6 (color online). The $\nu_\mu \rightarrow \nu_\mu$ (left) and $\nu_\mu \rightarrow \nu_e$ (right) oscillation probabilities, plotted in path length vs neutrino energy for the c^{TT} parameter in the (top to bottom) $e\mu$, $\mu\tau$, and $e\tau$ sectors. The c^{TT} coefficients scale terms proportional to LE , so the distortions get stronger at higher energies.

APPENDIX C: ZENITH ANGLE DISTRIBUTIONS

This Appendix includes ratios relative to standard three-flavor oscillations for all of the subsamples included in the analysis. The ratios are generally plotted vs zenith angle ($\cos \theta_z$), except for samples which are binned only in energy. The data is shown as points with statistical error bars. The dashed lines represent the best fits for each of the six fits while the solid lines represent examples of large LV parameters (10^{-22} GeV and 7.5×10^{-23}), the same as the oscillograms in Appendix B). The plots are divided into e^- - and NC-like samples and μ -like samples, and the a^T and c^{TT} fits are shown separately (Figs. 7-8 and Figs. 9-10, respectively), and are divided into e^- - and NC-like samples (Figs. 7 and 9) and π^0 -like samples (Figs. 8 and 10).

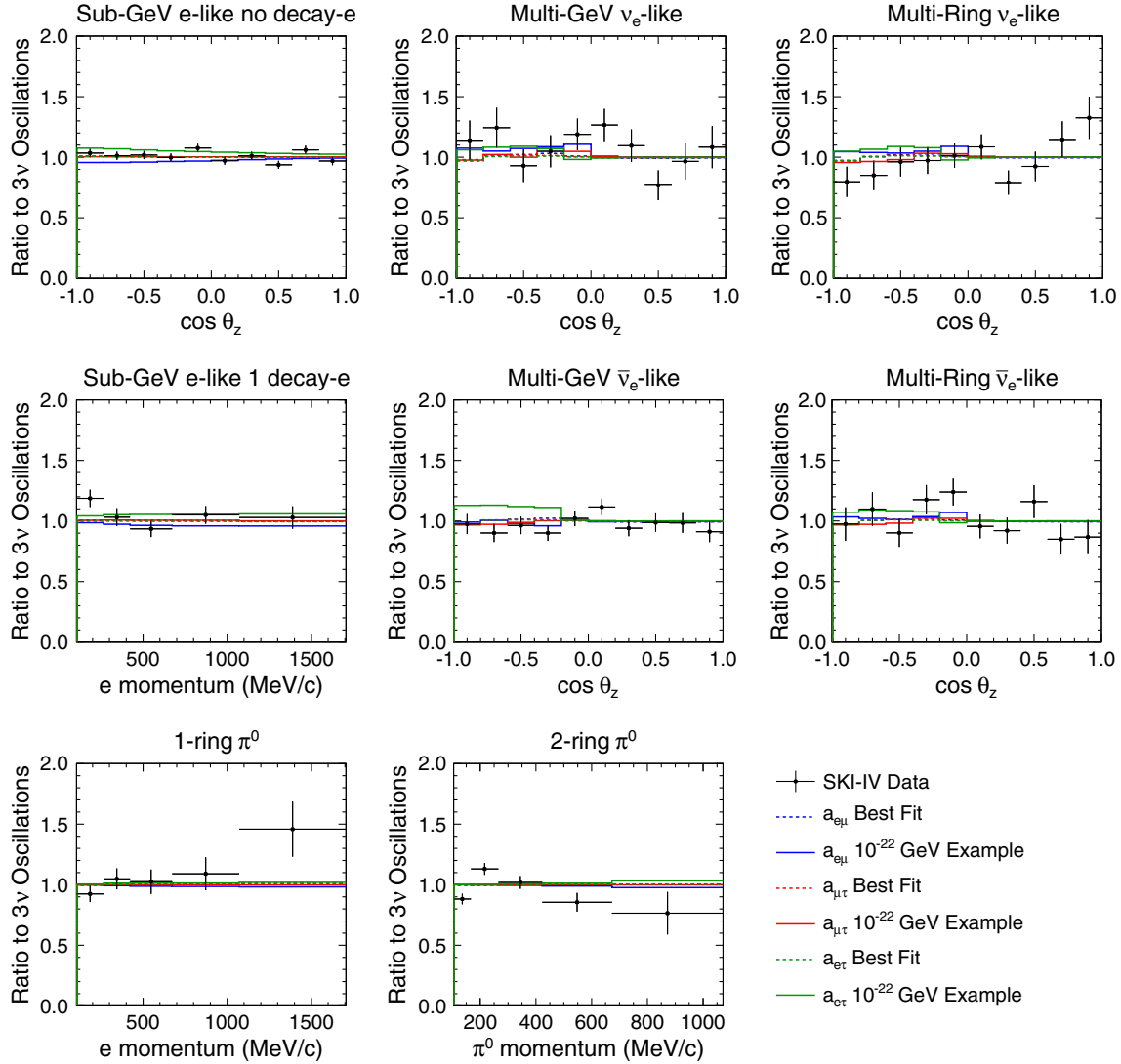


FIG. 7 (color online). Ratios of the summed SK-I through SK-IV $\cos \theta_z$ or momentum distributions relative to standard three-flavor oscillations of the e^- - and NC π^0 -like FC subsamples. They are projected into $\cos \theta_z$ when binned in both momentum and angle. The black points represent the data with statistical errors. The dashed lines represent the best fits from the three sectors for the a^T parameters and the solid lines represent examples of large Lorentz violation ($a^T = 10^{-22}$ GeV, equivalent to Fig. 5). Significant deviations from unity would indicate Lorentz violation.

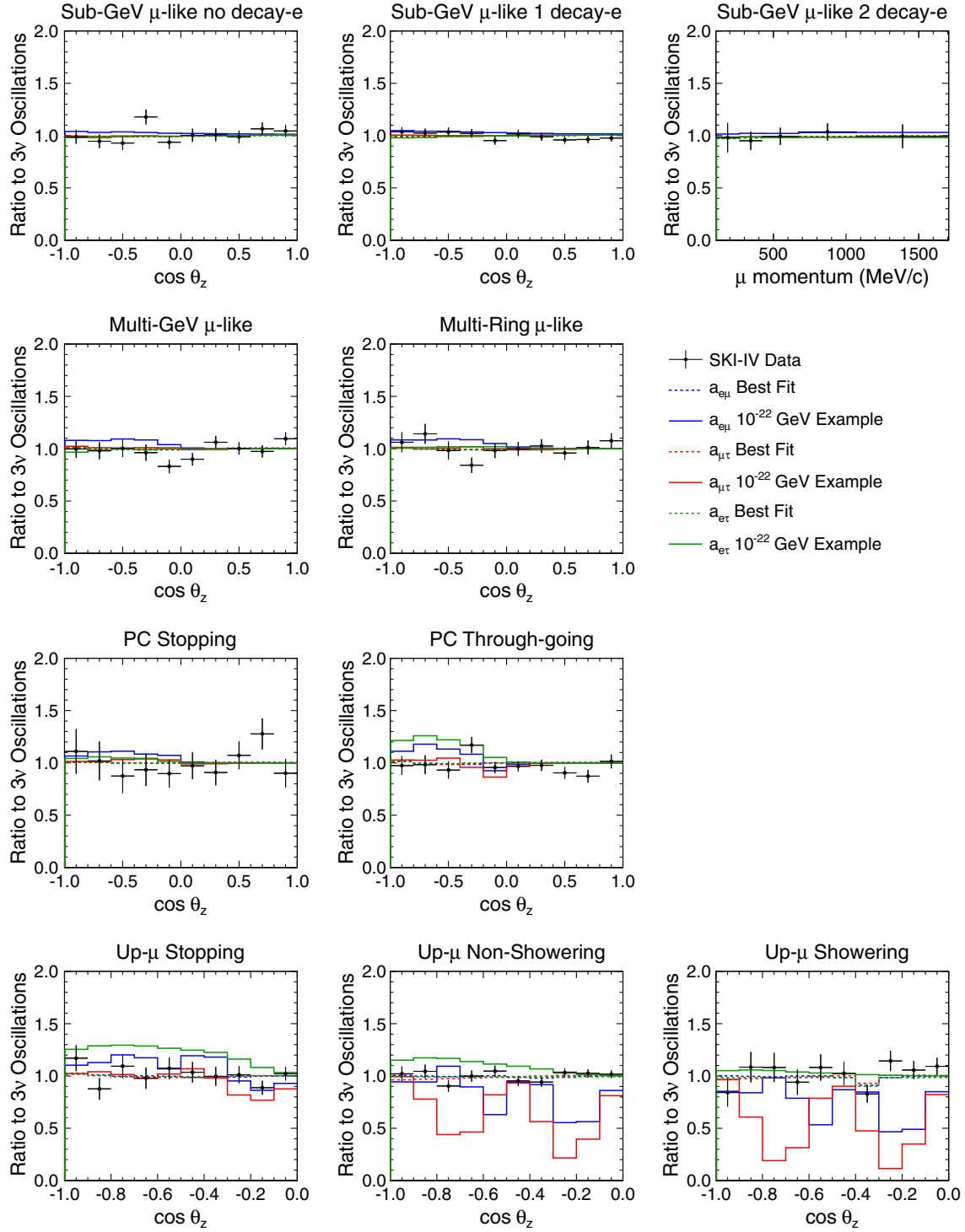


FIG. 8 (color online). Ratios of the summed SK-I through SK-IV $\cos \theta_z$ distributions relative to standard three-flavor oscillations for the μ -like FC, PC, and Up- μ subsamples. They are projected into $\cos \theta_z$ when binned in both momentum and angle and the Sub-GeV 2 decay-e sample is binned only in momentum. The black points represent the data with statistical errors. The dashed lines represent the best fits from the three sectors for the a^T parameters and the solid lines represent examples of large Lorentz violation ($a^T = 10^{-22}$ GeV, equivalent to Fig. 5). Significant deviations from unity would indicate Lorentz violation.

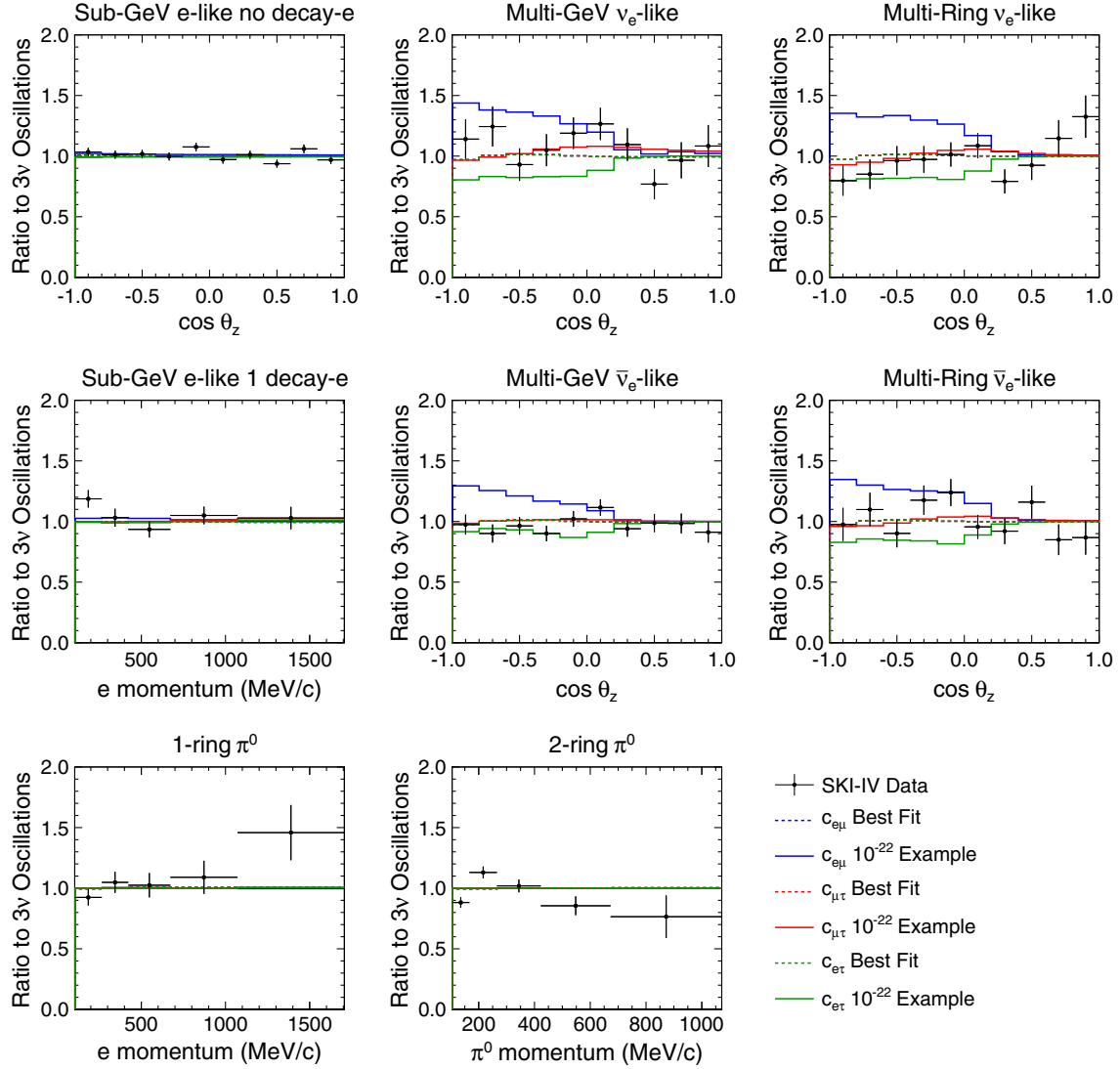


FIG. 9 (color online). Ratios of the summed SK-I through SK-IV $\cos \theta_z$ or momentum distributions relative to standard three-flavor oscillations of the e - and $\text{NC}\pi^0$ -like FC subsamples. They are projected into $\cos \theta_z$ when binned in momentum and angle. The black points represent the data with statistical errors. The dashed lines represent the best fits from the three sectors for the c^{TT} parameters and the solid lines represent examples of large Lorentz violation ($c^{TT} = 7.5 \times 10^{-23}$, equivalent to Fig. 6). Significant deviations from unity would indicate Lorentz violation.

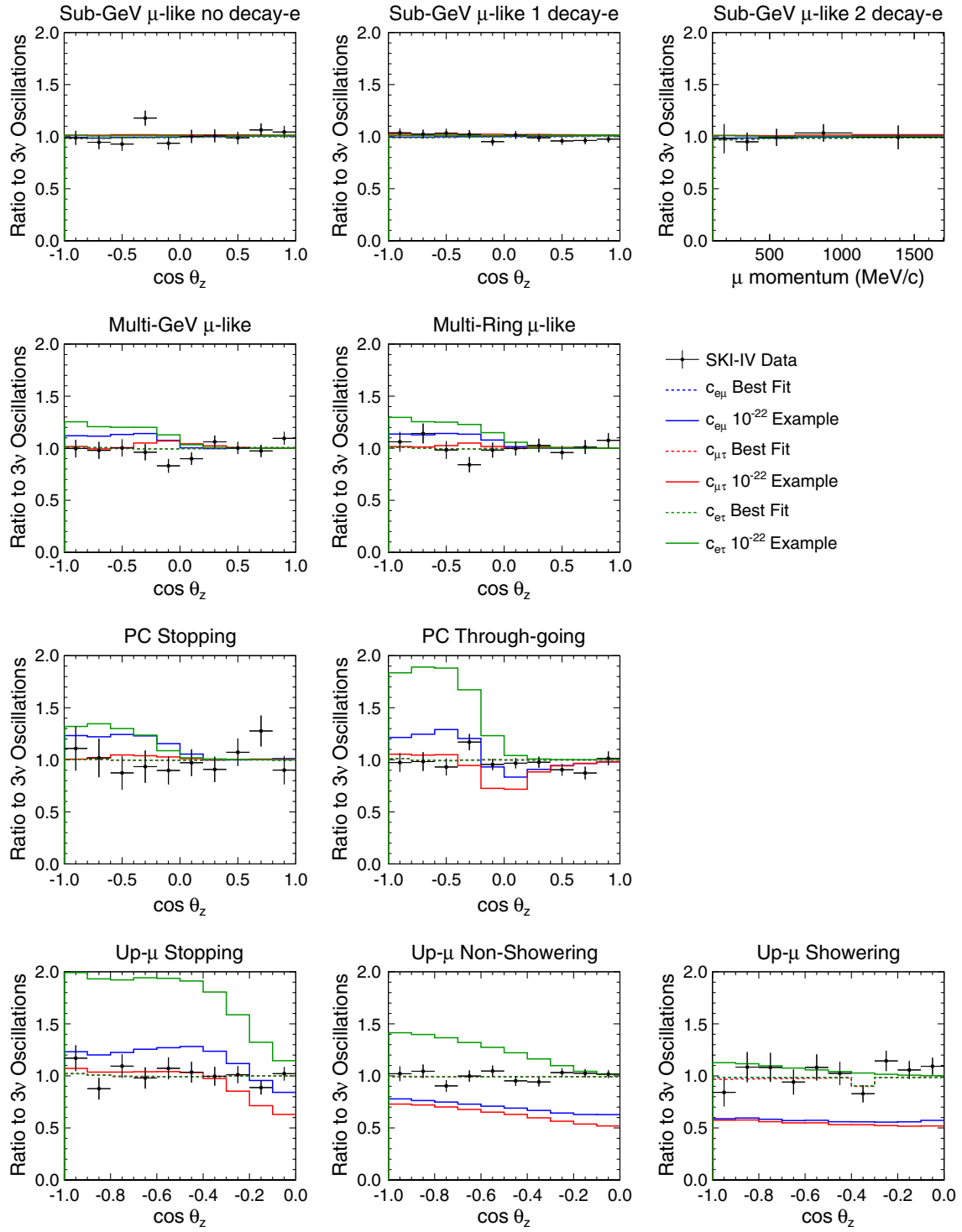


FIG. 10 (color online). Ratios of the summed SK-I through SK-IV $\cos \theta_z$ distributions relative to standard three-flavor oscillations for the μ -like FC, PC, and UP- μ subsamples. They are projected into $\cos \theta_z$ when binned in both and the Sub-GeV 2 decay-e sample is binned only in momentum. The black points represent the data with statistical errors. The dashed lines represent the best fits from the three sectors for the c^{TT} parameters and the solid lines represent examples of large Lorentz violation ($c^{TT} = 7.5 \times 10^{-23}$, equivalent to Fig. 6). Significant deviations from unity would indicate Lorentz violation.

- [1] V. A. Kostelecky and S. Samuel, Spontaneous breaking of Lorentz symmetry in string theory, *Phys. Rev. D* **39**, 683 (1989).
- [2] S. W. Hawking, Breakdown of predictability in gravitational collapse, *Phys. Rev. D* **14**, 2460 (1976).
- [3] R. Brustein, D. Eichler, and S. Foffa, Probing the Planck scale with neutrino oscillations, *Phys. Rev. D* **65**, 105006 (2002).
- [4] D. Colladay and V. A. Kostelecky, CPT violation and the standard model, *Phys. Rev. D* **55**, 6760 (1997).
- [5] D. Colladay and V. A. Kostelecky, Lorentz violating extension of the standard model, *Phys. Rev. D* **58**, 116002 (1998).
- [6] V. A. Kostelecky, Gravity, Lorentz violation, and the standard model, *Phys. Rev. D* **69**, 105009 (2004).
- [7] G. Amelino-Camelia, C. Lammerzahl, A. Macias, and H. Muller, The Search for quantum gravity signals, *AIP Conf. Proc.* **758**, 30 (2005).
- [8] R. Bluhm, Overview of the SME: implications and phenomenology of Lorentz violation, *Lect. Notes Phys.* **702**, 191 (2006).
- [9] O. W. Greenberg, CPT violation implies violation of Lorentz invariance, *Phys. Rev. Lett.* **89**, 231602 (2002).
- [10] While LV can exist without CPT violation, CPT violation requires LV.
- [11] V. A. Kostelecky and M. Mewes, Lorentz violation and short-baseline neutrino experiments, *Phys. Rev. D* **70**, 076002 (2004).
- [12] V. A. Kostelecky and N. Russell, Data tables for Lorentz and CPT violation, *Rev. Mod. Phys.* **83**, 11 (2011). The numbers compared here come from a newer version than the published version, [arXiv:0801.0287v8](https://arxiv.org/abs/0801.0287v8).
- [13] D. Mattingly, Modern tests of Lorentz invariance, *Living Rev. Relativity* **8**, 5 (2005).
- [14] *CPT and Lorentz symmetry. Proceedings: CPT'98, Bloomington, USA, 1998*, edited by V. Kostelecky (World Scientific, Singapore, 1999); *CPT and Lorentz symmetry. Proceedings: 2nd Meeting, Bloomington, USA, 2001*, edited by V. Kostelecky (2002); *CPT and Lorentz symmetry. Proceedings: 3rd Meeting, Bloomington, USA, 2004*, edited by V. Kostelecky (2005); *CPT and Lorentz symmetry. Proceedings: 4th Meeting, Bloomington, USA, 2007*, edited by V. Kostelecky (2008).
- [15] V. A. Kostelecky and M. Mewes, Neutrinos with Lorentz-violating operators of arbitrary dimension, *Phys. Rev. D* **85**, 096005 (2012).
- [16] V. A. Kostelecky and M. Mewes, Lorentz and CPT violation in the neutrino sector, *Phys. Rev. D* **70**, 031902 (2004).
- [17] V. A. Kostelecky and M. Mewes, Lorentz and CPT violation in neutrinos, *Phys. Rev. D* **69**, 016005 (2004).
- [18] L. B. Auerbach *et al.* (LSND Collaboration), Tests of Lorentz violation in anti- $\nu(\mu)$ and anti- $\nu(e)$ oscillations, *Phys. Rev. D* **72**, 076004 (2005).
- [19] A. A. Aguilar-Arevalo *et al.* (MiniBooNE Collaboration), Test of Lorentz and CPT violation with short baseline neutrino oscillation excesses, *Phys. Lett. B* **718**, 1303 (2013).
- [20] P. Adamson *et al.* (MINOS Collaboration), Testing Lorentz Invariance and CPT Conservation with NuMI Neutrinos in the MINOS Near Detector, *Phys. Rev. Lett.* **101**, 151601 (2008).
- [21] P. Adamson *et al.* (MINOS Collaboration), Search for Lorentz invariance and CPT violation with muon antineutrinos in the MINOS Near Detector, *Phys. Rev. D* **85**, 031101 (2012).
- [22] P. Adamson *et al.* (MINOS Collaboration), A Search for Lorentz Invariance and CPT Violation with the MINOS Far Detector, *Phys. Rev. Lett.* **105**, 151601 (2010).
- [23] B. Rebel and S. Mufson, The search for Neutrino-Antineutrino mixing resulting from Lorentz invariance violation using neutrino interactions in MINOS, *Astropart. Phys.* **48**, 78 (2013).
- [24] Y. Abe *et al.* (Double Chooz Collaboration), First test of Lorentz violation with a reactor-based antineutrino experiment, *Phys. Rev. D* **86**, 112009 (2012).
- [25] J. S. Diaz, T. Katori, J. Spitz, and J. Conrad, Search for neutrino-antineutrino oscillations with a reactor experiment, *Phys. Lett. B* **727**, 412 (2013).
- [26] R. Abbasi *et al.* (IceCube Collaboration), Search for a Lorentz-violating sidereal signal with atmospheric neutrinos in IceCube, *Phys. Rev. D* **82**, 112003 (2010).
- [27] J. S. Diaz, V. A. Kostelecky, and M. Mewes, Perturbative Lorentz and CPT violation for neutrino and antineutrino oscillations, *Phys. Rev. D* **80**, 076007 (2009).
- [28] Y. Fukuda *et al.* (Super-Kamiokande Collaboration), The Super-Kamiokande detector, *Nucl. Instrum. Methods Phys. Res., Sect. A* **501**, 418 (2003).
- [29] T. Akiri, Sensitivity of atmospheric neutrinos in Super-Kamiokande to Lorentz violation, at the Sixth Meeting on CPT and Lorentz Symmetry, Bloomington, Indiana, 2013, [arXiv:1308.2210](https://arxiv.org/abs/1308.2210).
- [30] Y. Fukuda *et al.* (Super-Kamiokande Collaboration), Evidence for oscillation of atmospheric neutrinos, *Phys. Rev. Lett.* **81**, 1562 (1998).
- [31] Y. Ashie *et al.* (Super-Kamiokande Collaboration), Evidence for an oscillatory signature in atmospheric neutrino oscillation, *Phys. Rev. Lett.* **93**, 101801 (2004).
- [32] K. Abe *et al.* (Super-Kamiokande Collaboration), Solar neutrino results in Super-Kamiokande-III, *Phys. Rev. D* **83**, 052010 (2011).
- [33] B. T. Cleveland, T. Daily, R. Davis Jr, J. R. Distel, K. Lande, C. K. Lee, P. S. Wildenhain, and J. Ullman, Measurement of the solar electron neutrino flux with the Homestake chlorine detector, *Astrophys. J.* **496**, 505 (1998).
- [34] J. N. Abdurashitov *et al.* (SAGE Collaboration), Measurement of the solar neutrino capture rate with gallium metal. III: Results for the 2002–2007 data-taking period, *Phys. Rev. C* **80**, 015807 (2009).
- [35] M. Altmann *et al.* (GNO Collaboration), Complete results for five years of GNO solar neutrino observations, *Phys. Lett. B* **616**, 174 (2005).
- [36] W. Hampel *et al.* (GALLEX Collaboration), GALLEX solar neutrino observations: Results for GALLEX IV, *Phys. Lett. B* **447**, 127 (1999).
- [37] B. Aharmim *et al.* (SNO Collaboration), Combined analysis of all three phases of solar neutrino data from the Sudbury Neutrino Observatory, *Phys. Rev. C* **88**, 025501 (2013).

- [38] S. Abe *et al.* (KamLAND Collaboration), Precision measurement of neutrino oscillation parameters with KamLAND, *Phys. Rev. Lett.* **100**, 221803 (2008).
- [39] F. P. An *et al.* (DAYA-BAY Collaboration), Observation of electron-antineutrino disappearance at Daya Bay, *Phys. Rev. Lett.* **108**, 171803 (2012).
- [40] Y. Abe *et al.* (Double Chooz Collaboration), First measurement of θ_{13} from delayed neutron capture on hydrogen in the double chooz experiment, *Phys. Lett. B* **723**, 66 (2013).
- [41] J. K. Ahn *et al.* (RENO collaboration), Observation of Reactor Electron Antineutrino Disappearance in the RENO Experiment, *Phys. Rev. Lett.* **108**, 191802 (2012).
- [42] M. H. Ahn *et al.* (K2K Collaboration), Measurement of neutrino oscillation by the K2K experiment, *Phys. Rev. D* **74**, 072003 (2006).
- [43] P. Adamson *et al.* (MINOS Collaboration), Measurement of Neutrino and Antineutrino Oscillations Using Beam and Atmospheric Data in MINOS, *Phys. Rev. Lett.* **110**, 251801 (2013).
- [44] K. Abe *et al.* (T2K Collaboration), First muon-neutrino disappearance study with an off-Axis beam, *Phys. Rev. D* **85**, 031103 (2012).
- [45] K. Abe *et al.* (Super-Kamiokande Collaboration), Evidence for the Appearance of Atmospheric Tau Neutrinos in Super-Kamiokande, *Phys. Rev. Lett.* **110**, 181802 (2013).
- [46] K. Abe *et al.* (T2K Collaboration), Evidence of electron neutrino appearance in a muon neutrino beam, *Phys. Rev. D* **88**, 032002 (2013).
- [47] N. Agafonova *et al.* (OPERA Collaboration), New results on $\nu_{\mu} \rightarrow \nu_{\tau}$ appearance with the OPERA experiment in the CNGS beam, *J. High Energy Phys.* **11** (2013) 036.
- [48] L. Wolfenstein, Neutrino oscillations in matter, *Phys. Rev. D* **17**, 2369 (1978); S. P. Mikheyev and A. Y. Smirnov, Resonant neutrino oscillations in matter, *Prog. Part. Nucl. Phys.* **23**, 41 (1989).
- [49] S. Desai *et al.* (Super-Kamiokande Collaboration), Study of TeV neutrinos with upward showering muons in Super-Kamiokande, *Astropart. Phys.* **29**, 42 (2008).
- [50] Y. Ashie *et al.* (Super-Kamiokande Collaboration), A Measurement of atmospheric neutrino oscillation parameters by SUPER-KAMIOKANDE I, *Phys. Rev. D* **71**, 112005 (2005).
- [51] R. Wendell *et al.* (Super-Kamiokande Collaboration), Atmospheric neutrino oscillation analysis with sub-leading effects in Super-Kamiokande I, II, and III, *Phys. Rev. D* **81**, 092004 (2010).
- [52] K. Abe *et al.* (Super-Kamiokande Collaboration), Limits on sterile neutrino mixing using atmospheric neutrinos in Super-Kamiokande, [arXiv:1410.2008](https://arxiv.org/abs/1410.2008) [to be published (*Phys. Rev. D*)].
- [53] K. Abe, Y. Hayato, T. Iida, K. Iyogi, J. Kameda *et al.*, Calibration of the Super-Kamiokande Detector, *Nucl. Instrum. Methods Phys. Res., Sect. A* **737**, 253 (2014).
- [54] Z. Maki, M. Nakagawa, and S. Sakata, Remarks on the unified model of elementary particles, *Prog. Theor. Phys.* **28**, 870 (1962).
- [55] A. M. Dziewonski and D. L. Anderson, Preliminary reference earth model, *Phys. Earth Planet. Interiors* **25**, 297 (1981).
- [56] W. Wang, Studies of non-standard effects in atmospheric neutrino oscillations of Super-Kamiokande, Ph.D. thesis, Boston University, 2007.
- [57] V. D. Barger, K. Whisnant, S. Pakvasa, and R. J. N. Phillips, Matter Effects on Three-Neutrino Oscillations, *Phys. Rev. D* **22**, 2718 (1980).
- [58] G. L. Fogli, E. Lisi, A. Marrone, D. Montanino, and A. Palazzo, Getting the most from the statistical analysis of solar neutrino oscillations, *Phys. Rev. D* **66**, 053010 (2002).
- [59] K. Abe *et al.* (T2K Collaboration), Precise Measurement of the Neutrino Mixing Parameter θ_{23} from Muon Neutrino Disappearance in an Off-axis Beam, *Phys. Rev. Lett.* **112**, 181801 (2014).
- [60] J. Beringer *et al.* (Particle Data Group), Review of Particle Physics (RPP), *Phys. Rev. D* **86**, 010001 (2012).
- [61] T. Katori (MiniBooNE Collaboration), Tests of Lorentz and CPT violation with MiniBooNE neutrino oscillation excesses, *Mod. Phys. Lett. A* **27**, 1230024 (2012).
- [62] T. Katori and J. Spitz, in *CPT and Lorentz Symmetry VI* (World Scientific, Singapore, 2014).
- [63] J. S. Diaz, IUHET Report No. 585 (to be published).